Theor Chem Acc (2013) 132:1331
DOI 10.1007/s00214-013-1331-2

REGULAR ARTICLE

A theoretical analysis of the magnetic properties of the low-dimensional copper(II)X_2(2-X-3-methylpyridine)$_2$ (X = Cl and Br) complexes

Sergi Vela · Mercè Deumal · Mark M. Turnbull · Juan J. Novoa

Received: 14 November 2012 / Accepted: 3 January 2013 / Published online: 5 February 2013

Abstract The First-principles Bottom-up (FPBU) procedure is applied to rationalize the different macroscopic magnetic properties of two compounds that were expected to be isostructural: bis(2-bromo-3-methylpyridine)dibromocopper(II), **1**, whose crystals present dominant ferromagnetic interactions, and bis(2-chloro-3-methylpyridine)dichlorocopper(II), **2**, that shows dominant antiferromagnetic behavior. Our FPBU analysis concludes that **1** presents a dominant ferromagnetic interaction of 1.16 cm^{-1} and other two non-negligible smaller interactions of opposite sign (−0.11 and 0.13 cm^{-1}). Contrarily, the dominant radical-pair interaction in **2** is antiferromagnetic (−2.37 cm^{-1}), in addition to three other non-negligible smaller magnetic couplings (0.48, −0.29, and −0.20 cm^{-1}). In **1**, these magnetic interactions generate a 2D magnetic topology of isolated planes, each made of weakly interacting parallel ferromagnetic chains, while in **2** they generate a 2D magnetic topology that can be described as isolated parallel double-decker planes, each of them made by weakly connected antiferromagnetic dimers. The computed magnetic susceptibility curve that results after applying the FPBU procedure fully matches the experimental one in both systems. Furthermore, since in both systems, the weaker magnetic interactions are one order of magnitude smaller than the dominant coupling, the magnetic susceptibility curve does not vary significantly whether including all interactions or only the dominant ones. Thus, the FPBU analysis quantitatively traces down the origin of the different magnetic behavior of **1** and **2** as due to the change in sign of their dominant magnetic interactions. We have been able to connect such a change in nature of the dominant magnetic interaction with a change in the conformation of the ligands, which converts from *anti* in bis(2-bromo-3-methylpyridine) (**1**) to *syn* in bis(2-chloro-3-methylpyridine) (**2**), confirming the previous hypothesis.

Keywords Molecule-based magnetism · Theoretical calculations · Density functional theory · Magnetic dimensionality · Magnetic exchange interactions · Copper(II) coordination complexes

Published as part of the special collection of articles derived from the 8th Congress on Electronic Structure: Principles and Applications (ESPA 2012).

Electronic supplementary material The online version of this article (doi:10.1007/s00214-013-1331-2) contains supplementary material, which is available to authorized users.

S. Vela · M. Deumal · J. J. Novoa (✉)
Departament de Química Física and IQTCUB,
Facultat de Química, Universitat de Barcelona,
Martí i Franquès 1, 08028 Barcelona, Spain
e-mail: juan.novoa@ub.edu

M. M. Turnbull
Carlson School of Chemistry and Biochemistry,
Clark University, 950 Main St., Worcester,
MA 01610, USA

1 Introduction

Low-dimensional molecule-based magnets, materials where the observed magnetic exchange is limited to less than three dimensions over a broad range of temperatures, have become a major source of interest for the study of viable super exchange pathways and magneto-structural correlations. The advantage to the use of low-dimensional materials for magnetic study is clear; fewer interactions makes them easier to define and provides fewer parameters that affect the sign and magnitude of the magnetic interactions. However, for such studies to be effective, the true nature of the magnetic lattice must be known so that all

non-negligible interactions are taken into account. Low-dimensional materials are also interesting for the possible presence of new physical phenomena associated with their reduced dimensionality.

The problem with many studies of low-dimensional magnets is that the dimensionality of the magnetic lattice is generally assumed from the physical lattice (obtained from X-ray or neutron diffraction studies) and these may, or may not, correlate with the true dimensionality determined from more accurate and expensive physical measurements (e.g. muon spin rotation determinations). One prime example is that of $(VO)_2(P_2O_7)$ which was studied in detail as a magnetic ladder for nearly a decade [1–5] before neutron scattering experiments showed the material to be better described as an alternating magnetic chain [6, 7]. Magnetic dimensionality can also be accurately determined from accurate theoretical studies of the magnetic interactions within a crystal, as we show hereafter in the case of bis(2-bromo-3-methylpyridine)dibromocopper(II) (**1**) and bis(2-chloro-3-methylpyridine)dichlorocopper(II) (**2**) (see Fig. 1).

Despite the similar crystal structure of **1** and **2**, they exhibit very different macroscopic magnetic properties. As observed in experimental studies, [8] **1** is a molecule-based magnet whose magnetic susceptibility is fitted using a ferromagnetic chain model with weak antiferromagnetic interchain corrections, while the magnetic data of **2** is fitted to an isolated antiferromagnetic dimer model. It has been postulated that the reason for such a different magnetic behavior is the change in conformation that the $Cu(II)X_2(2\text{-}X\text{-}3\text{-}Mepy)_2$ (X = Cl, Br; Mepy = methylpyridine) radical centers show in **1** and **2**. Specifically, while in **1** all centers are present in the *anti*-conformation, in **2** all are found in the *syn*-conformation (see Fig. 1). However, this proposal has not yet been supported by theoretical studies on the magnetism of these two compounds. Our main aim in this work is to confirm the validity of such hypothesis by applying the First-principles Bottom-up (FPBU) procedure [9] to **1** and **2** in order to gain an in-depth insight into the nature of their magnetic interactions and, by comparing them, rationalize the origin of their difference.

The FPBU procedure computes the macroscopic magnetic properties of any molecule-based compound based only upon knowledge of the crystal structure. It begins by evaluating, using First-Principles methods (i.e. using high-level ab initio [10] or DFT [11] methods), the microscopic J_{AB} magnetic exchange parameters for all symmetry-unique radical-pairs in the crystal (note that these parameters uniquely define the Heisenberg Hamiltonian that describes the magnetic interactions within the crystal, in a pair approximation). The matrix representation of the Heisenberg Hamiltonian is then computed on a properly selected finite subset of the crystal (called the magnetic

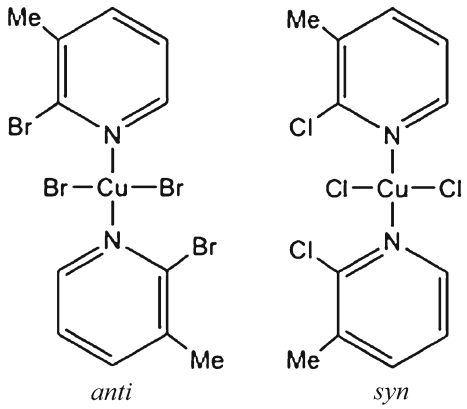

Fig. 1 Chemical structure of the *anti*-bis(2-bromo-3-methylpyridine)dibromocopper(II) (**1**) and *syn*-bis(2-chloro-3-methylpyridine) dichlorocopper(II) (**2**) conformers

model). Within a regionally reduced density matrix approach, the corresponding eigenvalues are obtained after diagonalization and used in the appropriate Statistical Mechanics expression of the property of interest, in this case the magnetic susceptibility, in order to evaluate such property in an unbiased and accurate form. The FPBU methodology has been previously shown to reproduce well the magnetic properties of molecule-based magnets presenting a wide variety of magnetic behaviors [12–16]. It also allows one to connect the macroscopic magnetic property of interest with its microscopic origin (i.e. the values of the J_{AB} magnetic couplings and the network of connections that the non-negligible J_{AB} interactions create among the radicals of the crystal, known as the *magnetic topology* of the crystal). The procedure is called *bottom-up* because the macroscopic magnetic properties are determined from the computed values of the microscopic radical···radical magnetic interactions, which are calculated using *first-principles* methods (no "a priory" assumptions are made about the size or topology of the magnetic interactions present in the crystal). In this paper, the FPBU procedure is used to identify in a numerical and unbiased way the origin of the different magnetic behavior of compounds **1** and **2**.

2 Methodological details

The *First-principles Bottom-up* FPBU procedure [9] is a four-step methodology that computes the macroscopic magnetic properties of a molecule-based crystalline material using its crystal structure as the only input. The four steps of the FPBU procedure can be summarized as follows (they are valid for any crystal, although in the description below they have been adapted to the case of compounds **1** and **2**):

1. *Identification of all unique radical···radical pairs within the crystal likely to be magnetically active.* All symmetry-unique radical-pairs (d_i), whose radical···radical distance is smaller than a given threshold, are identified by doing an in-depth analysis of the crystal. The threshold is selected in such a way that all relevant first and second nearest neighbor radical···radical pairs are included. No differences arise if the selected radical···radical magnetic interactions are through-bond or through-space [16].
2. *Calculation of the radical···radical magnetic interactions* (J_{AB}) *for all unique pairs found in Step 1.* The $Cu(II)X_2(2\text{-}X\text{-}3\text{-}Mepy)_2$ radicals present a doublet ground state. Thus, the strength of the magnetic interaction J_{AB} between any potentially relevant radical-pair d_i in a crystal can be calculated as $J_{AB} = (E^S_{BS} - E^T)$,[1] where E^T is the energy of the triplet, and E^S_{BS}, the energy of the open-shell singlet computed using the broken-symmetry approximation [17, 18]. The general Heisenberg Hamiltonian for a pair of A and B radicals

$$\hat{H} = -2\sum_{A,B} J_{AB}\hat{S}_A \cdot \hat{S}_B \qquad (1)$$

has been used, where $\hat{S}_A$ and $\hat{S}_B$ are the total spin operators acting on radicals A and B of each radical-pair. The radical-pair energies are computed at their crystal geometry. When available, it is recommended to use a crystal structure determined at a low temperature, where possible anisotropic thermal effects are minimized [19].

Note that the previous J_{AB} expression assumes that the overlap S_{ab} between the singly occupied molecular orbitals SOMOs of radicals A and B is small.[2] This hypothesis is valid in most through-space interactions, and also in some through-bond magnetic interactions (for instance, when the radical containing atoms are not directly bonded) [16]. The E^S_{BS} and E^T energies were evaluated using the UB3LYP [20–23] DFT functional, the Ahlrich's DZP basis set [24] for Cu, and the 6−31+G(*d*) basis set [25] on the remaining atoms. The choice of the B3LYP functional is based on previous studies that showed its performance to reproduce the experimental J_{AB} values and those from high-level ab initio methods on properly characterized systems [12–16]. The convergency criterion of the energy values was forced to have an accuracy of 10^{-7} au in order to guarantee an accuracy of 0.04 cm^{-1} in the J_{AB}'s values. All DFT calculations were carried out using GAUSSIAN09 [26].

Let us further comment on the information held by the SOMOs. In crystals of **1** and **2**, the magnetic interactions formally originate in the overlap between the SOMOs hosting the unpaired *d* electron in the tetracoordinated Cu(II) ions of the $Cu(II)X_2(2\text{-}X\text{-}3\text{-}Mepy)_2$ (X = Cl in **1** and X = Br in **2**) radicals (Fig. 2a). However, UB3LYP calculations indicate that in both radicals their SOMO, and therefore spin density, spreads over the Cu-coordinated halide atoms and also onto the Mepy nitrogen atoms bonded to the Cu(II) atom (see Fig. 2b, c). As magnetic interactions originate in the overlap between the occupied orbitals, and in particular the SOMO orbitals, the shape of the SOMO in isolated radicals of **1** and **2** suggests that the strongest magnetic pathways between their radical-pairs are expected to be those involving short-distance Cu···halide interactions, halide···halide interactions, and also (Mepy)N···N(Mepy) interactions.
3. *Determination of the magnetic topology of the crystal and selection of the appropriate model space.* The magnetic topology is straightforwardly defined by the network of connectivities among the spin centers linked by non-negligible $J_{AB}(d_i)$ interactions (previous tests have shown that when $|J_{AB}(d_i)| < 0.05$ cm^{-1}, the magnetic interaction can be considered as negligible). Once the magnetic topology of the full crystal is known, magnetic models can be selected, namely subsets of radicals whose propagation along the crystallographic axes reproduces the magnetic topology of the infinite crystal and includes all non-negligible J_{AB} magnetic interactions in a ratio as close as possible to that found in the infinite crystal. The smallest of those finite magnetic models is the minimal magnetic model. When the minimal magnetic model is properly defined, the macroscopic properties computed by enlarging it converge smoothly toward the computed data obtained using the minimal model and, in turn, toward the experimental results.
4. *Calculation of the macroscopic magnetic properties of the crystal.* In Step 2 of the FPBU procedure, from each two $S = ½$ radicals, the energies and therefore the magnetic interaction parameter (the J_{AB}) of the effective Hamiltonian are calculated. Then, all the values (i.e. energy eigenvalues and *S* quantum numbers) are mapped on the corresponding matrix elements of the model Hamiltonian, whose model space is selected in Step 3. In the present simple case, within the framework of a regionally reduced density matrix

[1] The criterion chosen to compute the energy difference is $E^S - E^T = 2(E^S_{BS} - E^T)/(1 + S_{ab})$. Open-shell singlet systems separate alpha spin density and beta spin density on different radicals. In our case, once the broken-symmetry approximation is applied, the resulting overlap S_{ab} between the alpha SOMO and the beta SOMO is zero. Thus, those orbitals are localized on each of the two radicals. This leads to $S_{ab} = 0$. As a conclusion, $J_{AB} = E^S_{BS} - E^T$.

[2] See footnote one.

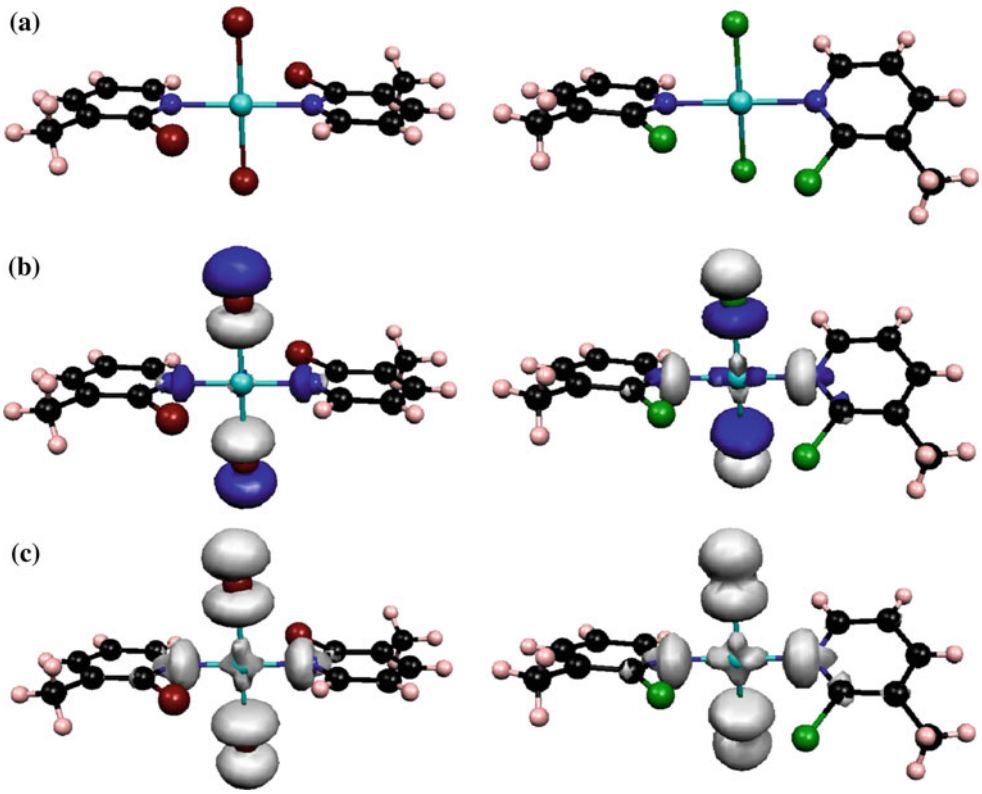

Fig. 2 **a** Molecular units of **1** (*left*) and **2** (*right*). **b** SOMO orbitals of isolated radicals of **1** and **2** (the isosurface of 0.03 au has been plotted; *blue* and *white* correspond to positive and negative regions, respectively). **c** Spin densities of monomers of **1** and **2** (the isosurface of 0.008 au has been plotted). *Color code*: Cu (*cyan*), N (*blue*), C (*black*), H (*pink*), Cl (*green*), Br (*brown*)

approach, the correspondence between model Hamiltonian and effective Hamiltonian is done by mapping the energies of the determinants on the diagonal elements of the Heisenberg Hamiltonian.[3] The energy eigenvalues and S quantum numbers obtained after full diagonalization of the matrix representation of (1) are then used to evaluate the magnetic properties of interest using the required statistical mechanics expressions (magnetization, heat capacity, magnetic susceptibility, etc.).

Note that the spectrum of the full crystal would require including all radical-pairs in the summation of Eq. 1, which is computationally impractical. Instead, it has been demonstrated [9] that a proper reproduction of the energy spectra is obtained by using a properly defined minimal magnetic model. If the radical is a doublet, as in compounds **1** and **2**, the size of the matrix representation increases with the number n of radicals in the model space as $n!/[(n/2)!(n/2)!]$. In practice, this means that we are limited to model spaces of 18 spin centers or fewer.

[3] Note that the model Hamiltonian in the context of magnetic interactions is the HDVV spin-only Hamiltonian, while the effective Hamiltonian is a projection onto an appropriate model space of calculations from the exact Hamiltonian.

3 Results and discussion

3.1 Crystal packing analysis of the crystals of **1** and **2**

The FPBU studies on crystals of **1** and **2** were done using the X-ray structures reported in the literature [8]. Both crystal structures have been obtained at low enough temperatures (120 K for **1** and 165 K for **2**) to expect the anisotropic contraction of the crystal to be minimized. This fact guarantees that the geometry of any radical-pair extracted from these crystal structures will be similar to the geometry for that pair at the low temperatures where magnetic collective phenomena are most evident (local maxima/minima) in most molecule-based magnets.

Both crystals belong to the $P\bar{1}$ space group and present similar cell parameters. The cell parameters for crystals of **1** are as follows: $a = 6.2440(2)$ Å, $b = 7.4588(3)$ Å, $c = 9.5897(4)$ Å, $\alpha = 104.777(2)°$, $\beta = 90.043(2)°$, $\gamma = 114.151(2)°$, $V = 391.24(3)$ Å^3. For crystals of **2** they are as follows: $a = 6.0949(4)$ Å, $b = 7.4718(4)$ Å, $c = 9.5654(5)$ Å, $\alpha = 104.579(2)°$, $\beta = 91.809(2)°$, $\gamma = 112.825(2)°$, $V = 384.47(6)$Å^3. However, as shown in Figs. 3 and 4, the relative arrangement of the radical molecules in each crystal is quite different. These differences are better appreciated in Fig. 4, when looking at their superstructure, that is, at the general arrangement of the radicals within the crystal, where each radical is only represented by its Cu atom. As observed in Fig. 4, the radicals

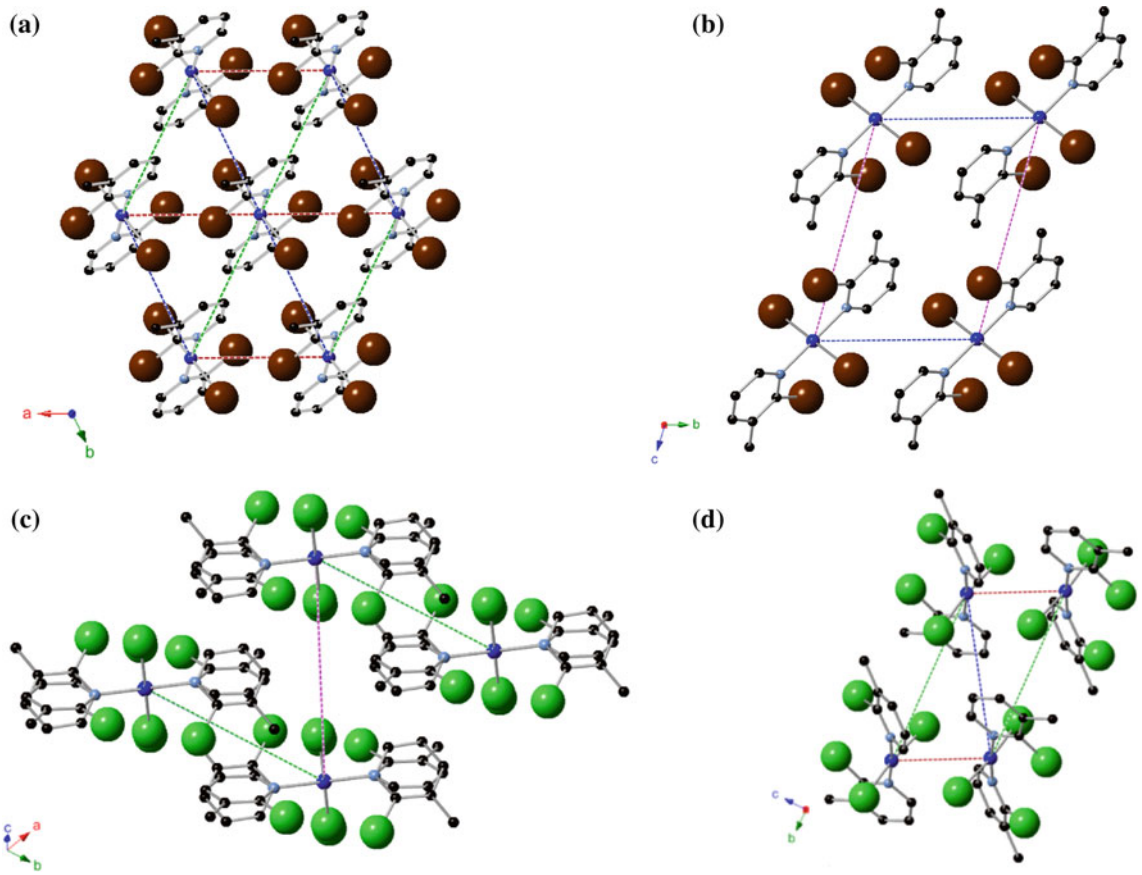

Fig. 3 For **1**, **a** top *ab*- and **b** lateral *bc*-views of the geometry of d_1–d_4 radical-pairs selected in Step 1 (see *dashed lines*). For **2**, **c** view along the $\alpha = 45°$, $\beta = 45°$, $\gamma = 45°$ direction and **d** lateral *bc*-view of the geometry of d_1–d_4 radical-pairs (see *dashed lines*). Hydrogen atoms have been removed for clarity. *Color code*: Cu (*deep-blue*), N (*blue*), C (*black*), Cl (*green*), Br (*brown*)

in **1** pack as stacks of flat planes, while in **2** they pack as stacks of double-decker corrugated planes, where each double-decker plane results from the aggregation of dimers.

3.2 First-principles bottom-up analysis of **1** and **2**

The results of applying the FPBU methodology to the study of the magnetic interactions in **1** and **2** are hereafter presented, grouped according to the four steps of the procedure.

Step 1 Identification of all unique radical···radical pairs from the crystal that are likely to be magnetically active.

All radical-pairs having a Cu···Cu distance shorter than 10 Å in both crystals were considered in **1** and **2** (the selected radical-pairs are numbered according to their Cu···Cu distance, d_1 being the dimer with the shortest distance). For **1**, four unique radical-pairs were found with Cu···Cu distances that range from 6.244 Å to 9.590 Å (see Fig. 5). For **2**, eleven unique radical-pairs were selected (see Supporting Information Figure S1 and Fig. 6 for magnetically relevant pairs). Their shortest Cu···Cu distance is 4.329 Å (d_1), while d_2–d_{11} present Cu···Cu distances ranging from 8 to 10 Å.

Step 2 Computation of the microscopic magnetic interactions, $J_{AB}(d_i)$, for all symmetry-unique radical-pairs selected in Step 1.

Calculation of the $J_{AB}(d_i)$ values done at the UB3LYP level (Table 1) indicates that **1** has only three magnetically non-negligible radical-pairs (i.e. $|J_{AB}(d_i)| > 0.05$ cm^{-1}): d_1, d_2, and d_3. The dominant radical-pair magnetic interaction is $J(d_2)$ (1.16 cm^{-1}), which is about one order of magnitude larger than $J(d_1)$ and $J(d_3)$ (−0.11 and 0.13 cm^{-1}, respectively). Note that our computed J_{AB} exchange coupling values are close to the experimental one, $J_{chain} = 0.89$ cm^{-1}, obtained by fitting the magnetic susceptibility curve with a ferromagnetic chain model with a correction term that was added to account for the weak interchain interactions (best fit value J'(interchain) = −0.25 cm^{-1})[4] [8]. As observed in Fig. 7a, the dominant magnetic interaction (d_2) is a through-space Cu–Br···Br–Cu interaction.

[4] Note that $J_{chain} = 0.89$ cm^{-1} corresponds to an experimentally fitted 2J parameter of 2.58 K. The J'(interchain) value has been translated from the fitted Curie–Weiss mean-field parameter theta (−0.74 cm^{-1}) assuming two neighbor radicals.

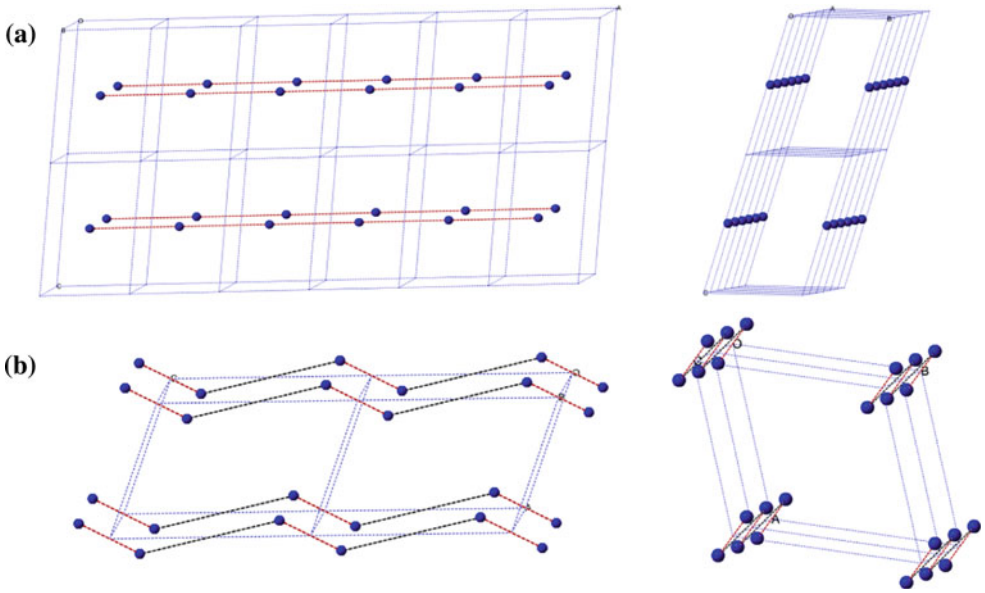

Fig. 4 Superstructure of **a 1** and **b 2**. Each radical is represented by its central Cu atom. The perfectly collinear chain in **1** (*red-dashed lines* in **a**) becomes corrugated in **2** and also non-regular since there is now a short Cu···Cu and a long Cu···Cu contact (*red-* and *black-dashed lines* in **b**, respectively)

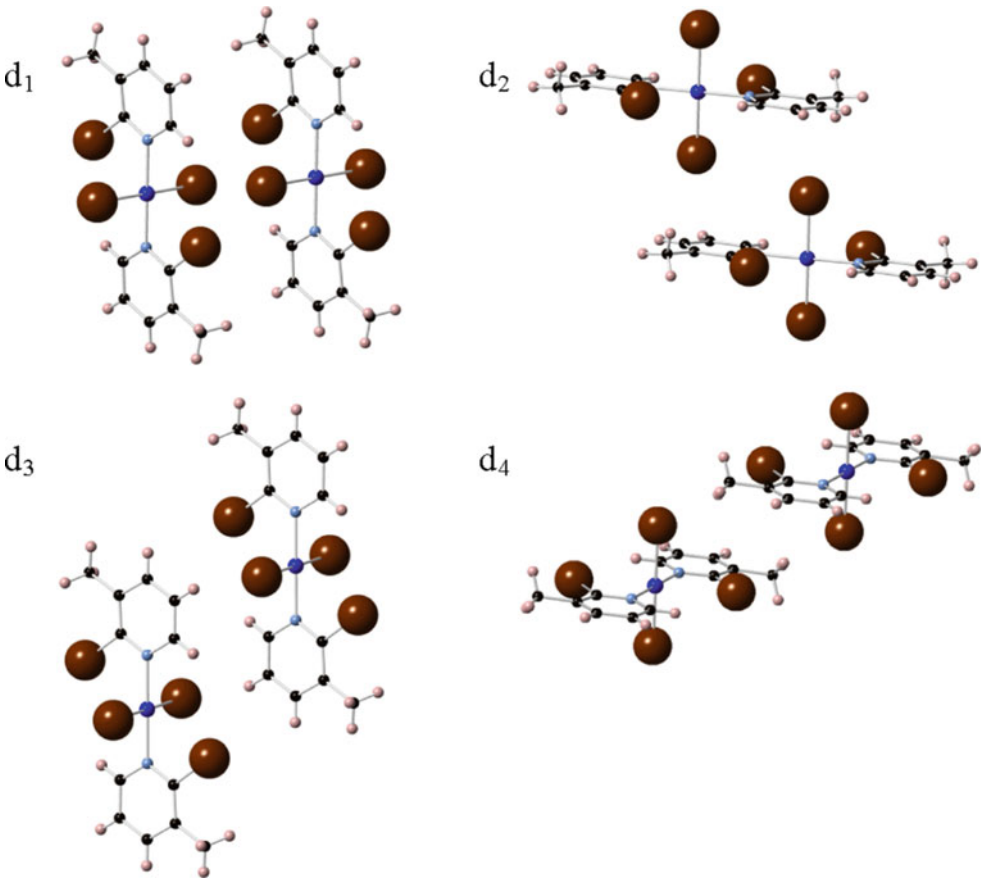

Fig. 5 Unique radical-pairs that present a Cu···Cu distance smaller than 10 Å in **1**

The values of the $J_{AB}(d_i)$ interactions computed at the UB3LYP level for the magnetically relevant radical-pairs in **2** are collected in Table 2 (see Fig. 6 for geometry of pairs). They show the presence of a dominant antiferromagnetic interaction, ($J(d_1) = -2.37$ cm^{-1}), which is almost one order of magnitude larger than the three remaining non-negligible magnetic couplings (0.48, −0.29, −0.20 cm^{-1}). These computed $J_{AB}(d_i)$ values compare well with those obtained by fitting the magnetic susceptibility curve of **2** with an isolated dimer model, $J_{dimer} =$

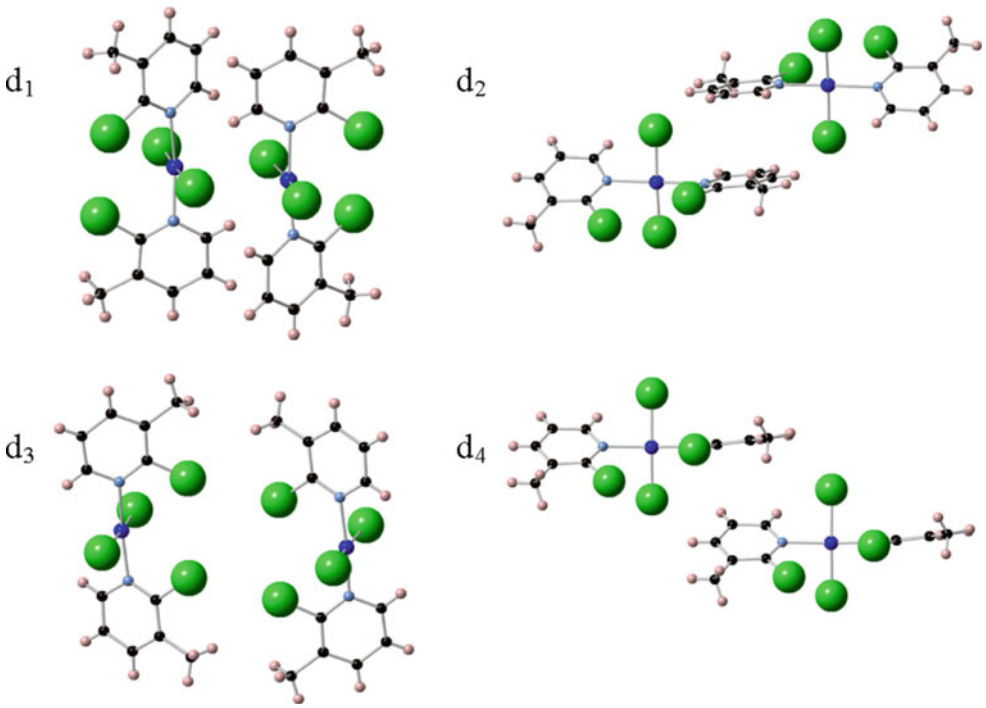

Fig. 6 Unique magnetically non-negligible radical-pairs that present a Cu···Cu distance smaller than 10 Å in **2**

Table 1 Values of the non-negligible magnetic exchange interaction parameter $J_{AB}(d_i)$ computed at the UB3LYP level for all unique radical-pairs present in **1**

Dimer	d(Cu···Cu)/Å	d(Br···Br)/Å	J_{AB}/cm^{-1}
d_1	6.244	5.253	−0.11
d_2	7.459	4.482	1.16
d_3	7.517	7.089	0.13

The values of the Cu···Cu and the shortest Cu–Br···Br–Cu distances are also given (in Å)

−2.72 cm^{-1} [8][5]. Let us further comment that, according to Fig. 7b, the dominant magnetic coupling (d_1) is a through-space magnetic interaction via a series of exchange pathways, ranging from Cu···Cu to Cu···Cl and Cl···Cl magnetic contacts.

The dominant ferromagnetic exchange observed in compound **1** is unusual as virtually all examples of magnetic superexchange via a two-halide pathway are antiferromagnetic. The reason for that could be the atypical orientation found for Br···Br interactions in **1** (see Fig. 7c, d). In **1**, the Cu–Br···Br angle of the dominant ferromagnetic radical-pair d_2 for this pathway is 106.4°, that is, close to 90°, which prevents any exchange coupling other than Br···Br. Whereas, in **2**, the Cu–Cl···Cl angle in the dominant antiferromagnetic pair d_1 is 62.8°, whose orientation allows Cu···Cu, Cu···Cl, and Cl···Cl magnetic exchange. The existence of regions of ferromagnetism in the Cu(II)-halide···halide-Cu(II) interactions present in crystals of Cu(II)X_2L_2 radicals studied here, suggest the need of a detailed study of their magneto-structural properties, but such study it is out of the scope of this paper.

Step 3 Determination of the magnetic topology of the crystal and selection of the appropriate magnetic model.

Figure 8 shows the 2D magnetic topology for the crystals of **1** and **2**. According to Fig. 8a, the network of magnetic interactions in **1** consists of a set of isolated ferromagnetic chains ($J(\mathbf{1}d_2) = 1.16$ cm^{-1}, blue solid lines), which pack forming planes of parallel chains ($J(\mathbf{1}d_1) = -0.11$ and $J(\mathbf{1}d_3) = 0.13$ cm^{-1}, red and green solid lines, respectively). Finally, the planes of chains stack in the third dimension with no magnetic linkages (see Fig. 8a). On the other hand, the magnetic topology of **2** (see Fig. 8b) consists of antiferromagnetic dimers ($J(\mathbf{2}d_1) = -2.37$ cm^{-1} in red solid lines), which then weakly interact to give rise to a stack of magnetically isolated double-decker planes ($J(\mathbf{2}d_2) = -0.29$, $J(\mathbf{2}d_3) = 0.48$ and $J(\mathbf{2}d_4) = -0.20$ cm^{-1} in blue, green, and purple solid lines, respectively). All these results confirm the expectations put forward on the basis of geometrical considerations [8], namely (1) the strongest interactions of **1**, $J(\mathbf{1}d_2)$, are ferromagnetic and run along a chain motif, (2) adjacent chains in **1** are weakly interconnected, although the interchain interactions are not just antiferromagnetic, but both antiferromagnetic $J(\mathbf{1}d_1)$ and ferromagnetic $J(\mathbf{1}d_3)$ in nature, and (3) the strongest

[5] Note that $J_{dimer} = -2.72$ cm^{-1} corresponds to an experimentally fitted 2J parameter of ca. −7.824 K.

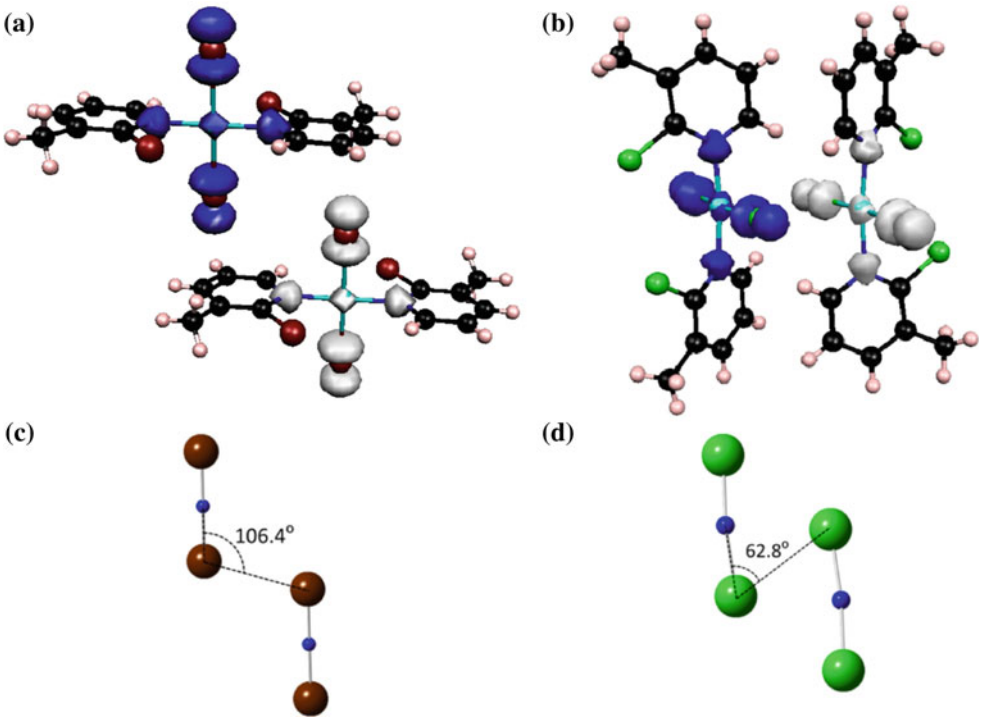

Fig. 7 Spin density of **a** d_2 in **1** and **b** d_1 in **2**. Local geometry of the (X–Cu–X)···(X–Cu–X) moiety for **c** d_2 in **1** and **d** d_1 in **2**. *Color code*: Cu (*deep-blue*), N (*blue*), C (*black*), Cl (*green*), Br (*brown*)

Table 2 Values of the non-negligible magnetic exchange interaction parameter $J_{AB}(d_i)$ computed at the UB3LYP level on all unique radical-pairs present in **2**

Dimer	d(Cu···Cu)/Å	d(Cl···Cl)/Å	J_{AB}/cm^{-1}
d_1	4.329	3.652	−2.37
d_2	8.071	7.559	−0.29
d_3	8.680	6.762	0.48
d_4	9.519	5.346	−0.20

The values of the Cu···Cu and shortest Cu–Cl···Cl–Cu distances are also given (in Å)

coupling in **2**, $J(\mathbf{2}d_1)$, yields antiferromagnetic dimers, although there are interdimer interactions which are both ferro- ($J(\mathbf{2}d_3)$) and antiferromagnetic ($J(\mathbf{2}d_2)$ and $J(\mathbf{2}d_4)$) that the geometrical considerations did not account for.

Step 4 Calculation of the macroscopic magnetic properties of the crystal.

The macroscopic magnetic susceptibility of **1** and **2** can now be computed from the energy spectrum of the Heisenberg Hamiltonian acting on a given magnetic model space, after substituting the $J_{AB}(d_i)$ interactions by their values in Tables 1 and 2, respectively. It thus follows that one first has to select a proper model space. Analysis of the magnetic topologies of **1** and **2** allows a proper selection of adequate magnetic models (Fig. 9). At this point, let us recall that the larger the magnetic model, the better the agreement between computed and experimental data is expected to be, but also at the higher computational cost of evaluating the macroscopic properties. The magnetic models were also selected keeping in mind that the ratio of J_i/J_j in the minimal model space should be as close as possible to that found in the full crystal, whatever the i and j radical-pair.

For compound **1**, four magnetic models were selected. The first one was the 2×(2×4) model (Fig. 9a), representing two (2×4)-radical centers from two adjacent planes. The second one, the 1×(2×4) model (Fig. 9b), was chosen to show that the magnetic susceptibility calculated on two planes (2×(2×4) model) is equivalent to that calculated for just one of those planes since they are magnetically isolated, at a reduced computational cost. Finally, the third is a 1×(2×8) model (Fig. 9c), chosen to test the convergence along the crystallographic directions along which the dominant magnetic interactions propagate. Note that this last model allows comparison with the literature data since the fitting model used experimentally was a chain model J(chain) that included a Curie–Weiss-term to account for weak interchain interactions J'(interchain).

Figure 9d–g show the magnetic models selected for compound **2**. Figure 9d shows the minimal magnetic model, the 2×2(2×2) model, which contains 16 spin centers and reproduces, by expansion, the double-decker topology of the full crystal. Similarly to the process followed in compound **1**, we included the 1×2(2×2) model (Fig. 9e) to test whether using a single double-decker model is appropriate or not as no magnetic interactions have been computed between adjacent double-decker

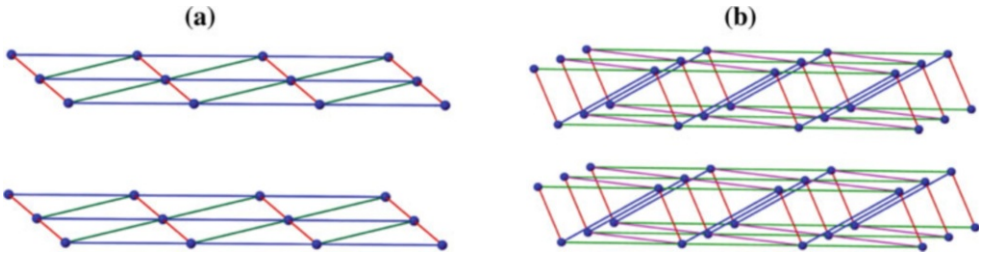

Fig. 8 Computed magnetic topologies for compounds **a 1** and **b 2**. *Color code* (common to **a** and **b**): $J(d_1)$ in *red*, $J(d_2)$ in *blue*, $J(d_3)$ in *green*, $J(d_4)$ in *purple*

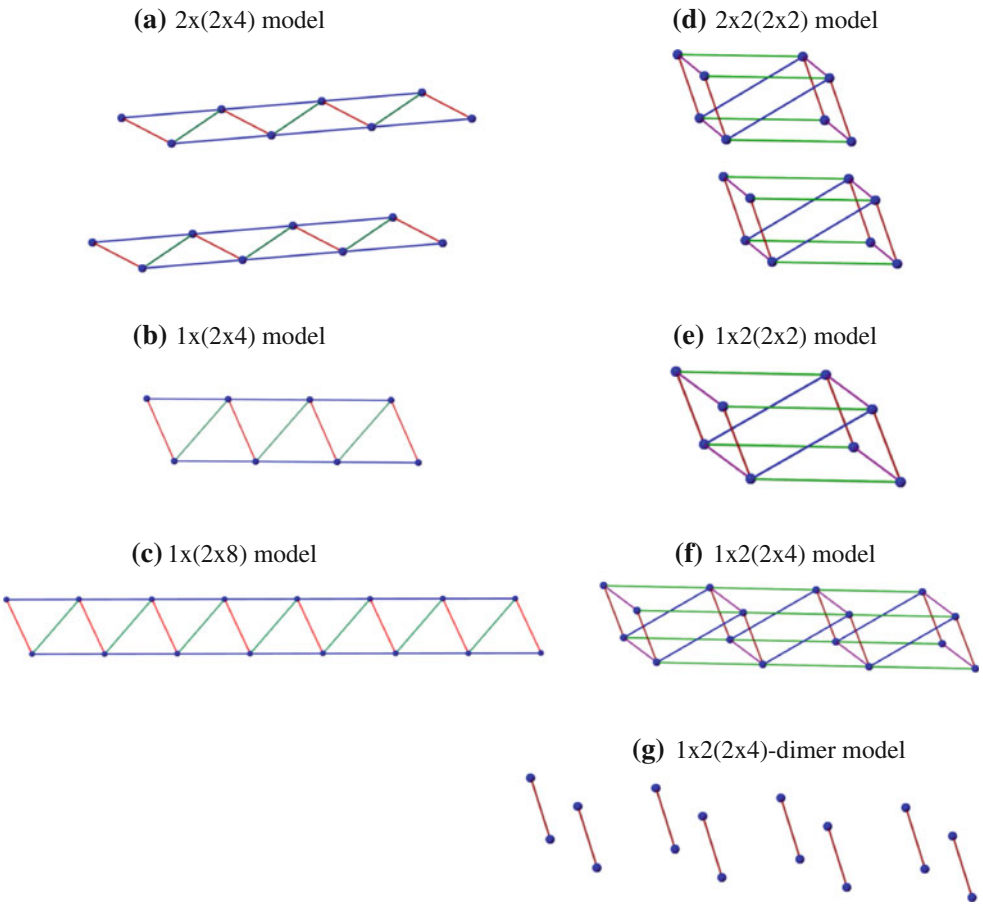

Fig. 9 Magnetic models used to compute the magnetic susceptibility *curves* for **1** (**a**–**c**) and **2** (**d**–**g**). *Blue dots* represent the Cu atoms of each radical. *Red*, *blue*, *green* and *purple lines* (see Fig. 8 for *color code*) represent the magnetic exchange interactions $J_{AB}(d_i)$ computed in *Step 2*

planes. The third model studied is the 1×2(2×4) (Fig. 9f), aimed at getting convergence in each of the planes along one direction. Finally, we included the 1×2(2×4)-dimer model (Fig. 9g) that describes a set of non-interacting dimers, which is the model employed in the literature to fit the experimental J_{dimer} values (this is equivalent to setting the values for $J(d_2)$, $J(d_3)$ and $J(d_4)$ equal to zero).

The magnetic susceptibility χ(T) curves computed for **1** and **2** are shown in Fig. 10. For **1**, all models agree well with the experimental curve, and the computed χ(T) data virtually overlap the experimentally measured values. This is consistent with the fact that all models contain the dominant exchange parameter, $J(d_2)$, in exactly the same proportion relative to the crystal as a whole. In other words, the key information about the energy spectrum is determined by $J(d_2)$ and all remaining non-negligible $J_{AB}(d_i)$ only induce a small perturbation in that spectrum. The results also allow us to conclude that the ferromagnetic character of **1** originates in the ferromagnetic interaction along the two-halide bridge d_2 radical-pair.

A similar trend is observed for the magnetic susceptibility curves of compound **2**. Once again, the χ(T) curves computed with the 2×2×(2×2), 1×2×(2×2), 1×2×(2×4), and 1×2×(2×4)-dimer models nearly numerically reproduce the experimental curve. These results allow us to conclude that the antiferromagnetic character of **2** originates in the antiferromagnetic intradimer interaction $J(d_1)$. Once again, the contributions of the additional interdimer interactions are important to describe the magnetic topology of the molecule-based crystal but numerically

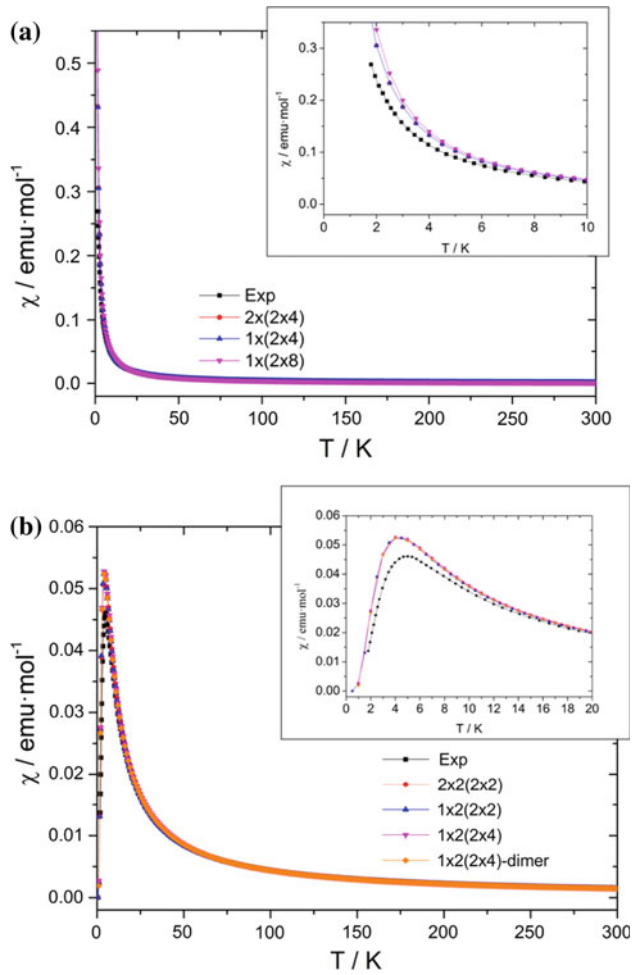

Fig. 10 Magnetic susceptibility curves computed for **a 1** and **b 2**. The *inset* shows a detailed view of the low temperature region of the *curve*. Note that in both compounds, the computed data overlap nearly exactly irrespective of the magnetic model used

negligible to compute χ(T), which is the magnetic property of interest.

3.3 The effect of conformation on the different magnetic behavior of **1** and **2**

The FPBU study carried out in this work helps in rationalizing the magnetic behavior of **1** and **2**. As it will be discussed, the experimental evidence regarding the magneto-structural relationship for these species is supported by the theoretical calculations presented in this work. A local difference in the conformation of the radical units (see Fig. 1 for *syn*- and *anti*-conformers) leads to a crucial change in the crystal packing and, thus, to the magnetic topology. This can be seen particularly in the d_1 pair that involves the shortest possible Cu···Cu distance between radicals. In **2**, the *syn* arrangement of the (2-Cl-3-Mepy) substituents in a monomer allows a second monomer to approach it along the non-sterically hindered face forming dimers at 4.329 Å (red solid line in Fig. 11b). This fact maximizes the overlap between the SOMO orbitals and enhances the antiferromagnetic interaction between them ($J(d_2) = -2.37$ cm^{-1}). Meanwhile, the closest adjacent monomer to the sterically hindered face is at 8.459 Å and no magnetic exchange interaction is found (red–white striped line in Fig. 11b).

On the other hand, in the brominated counterpart **1**, the *anti*-disposition of the (2-Br-3-Mepy) rings blocks any further coordination at both sterically hindered faces. This local arrangement results in a regular chain with a Cu···Cu distance of 6.244 Å between radicals ($J(d_1) = -0.11$ cm^{-1}, red solid line in Fig. 11a).

This behavior is known. A number of complexes of the general formula $Cu(S\text{-}py)_2X_2$, where S-py is an

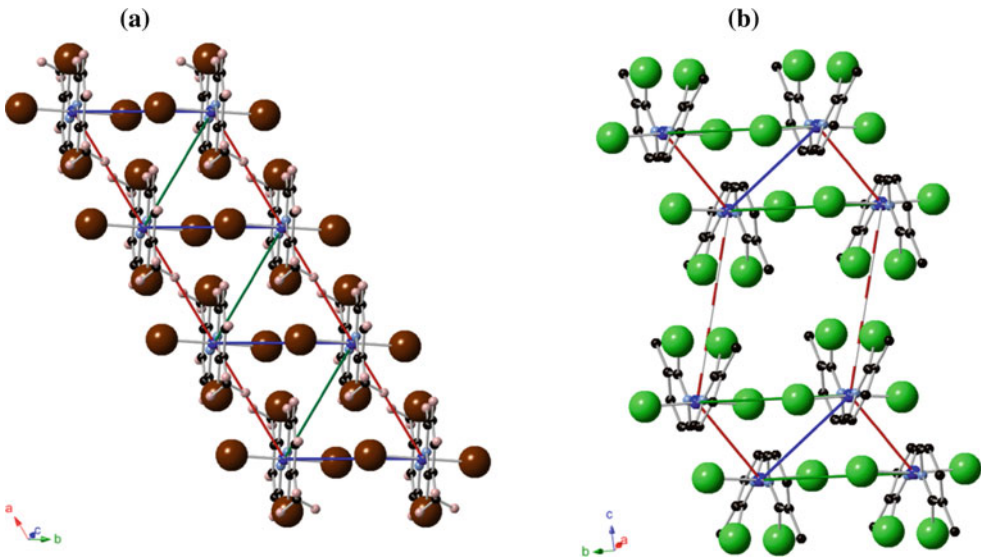

Fig. 11 Superimposed views of the crystal structure and the magnetic topology of **a 1** and **b 2**. Hydrogen atoms have been removed for clarity. *Color code* for atoms: Cu (*deep-blue*), N (*blue*), C (*black*), Cl (*green*), Br (*brown*)

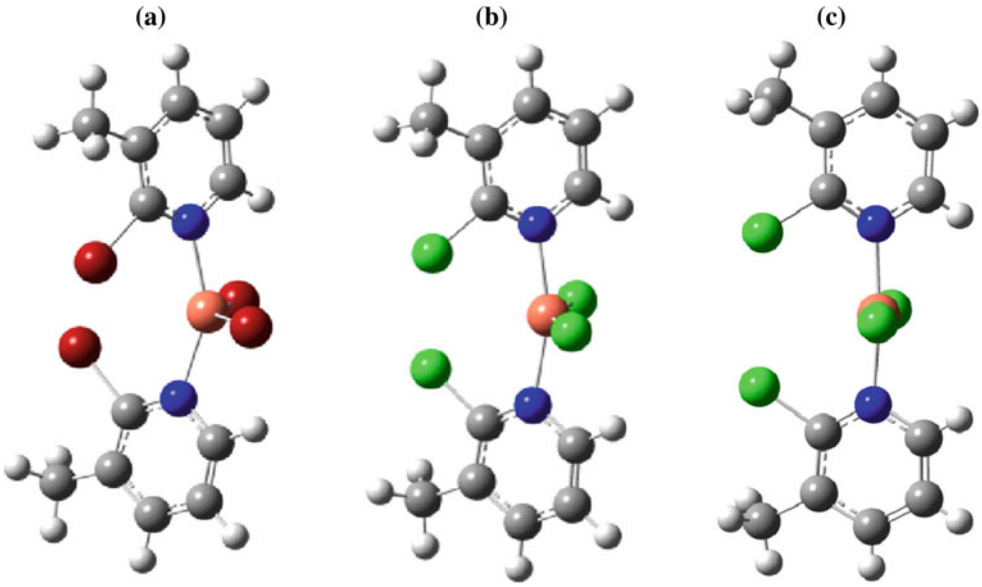

Fig. 12 Geometry of **a 1-opt**, **b 2-opt**, and **c 2**. *Color code* for atoms: Cu (*salmon*), N (*blue*), C (*grey*), H (*white*), Cl (*green*), Br (*brown*)

unsymmetrially substituted pyridine and X = Cl, Br, have been prepared and their structures fall into two categories: those which form chain-like structures (similar to **1**) [27–32] and those which form dimeric structures via short X···Cu contacts (similar to **2**) [28, 33, 34]. In all these cases, the relationship between the orientation of the substituents on the pyridine rings (*syn* or *anti*) and the structure holds; dimers are generated by *syn*-conformations and chains by *anti*-conformations. This is not surprising for 2-substituted pyridine ligands, but it also holds for 3-substituted pyridine ligands where the substituents are further from the metal center.

To elucidate whether this behavior can be ascribed to a local effect of the radical unit or to an effect of the crystal packing, we have conducted geometry optimizations of the (2-Cl-3-Mepy)$_2$CuCl$_2$ (**2-opt**) and (2-Br-3-Mepy)$_2$CuBr$_2$ (**1-opt**) monomers arranged in both the *syn*- and *anti*-conformations. In the gas phase, compounds **1-opt** and **2-opt** are more stable in the *syn* arrangement by 7.8 and 1.8 kcal mol^{-1}, respectively, which was expected for **2-opt** as it is the conformation present in the crystal but not for **1-opt**. Although an accurate study should be based on solid-state calculations performed on the crystal structure, a qualitative interpretation can be drawn from gas phase calculations on monomers.

According to the optimized geometries in the gas phase (Fig. 12a, b), the dihedral angle between (2-X-3-Mepy) rings is about 70° for **1-opt** and 54° for **2-opt**, indicating the preference of these monomers to be largely distorted from the planar 0° dihedral angle in the *syn* arrangement (Fig. 12c). The smaller distortion in **2-opt** is reduced to 30° in the crystalline structure of **2** indicating that the crystal packing seems to force the closure of the dihedral angle between rings. The larger distortion in **1-opt** can explain the absence of a *syn* polymorph as the crystals of **1** cannot accommodate such distortion.

In fact, within the (2-X-3-Mepy)CuX′$_2$ family of compounds, the heterohalide compound (2-Cl-3-Mepy)CuBr$_2$ with Cl atoms attached to the Mepy ring, reported in the same experimental work [8], shows both types of conformations in its polymorphs: *syn*-dimers and *anti*-chains. This indicates that, when X is Cl, the difference in stability between the *syn*-and *anti*-conformers is small enough to obtain a mixture of them, irrespective of X′ being Br. In view of these data, it appears that the key factor responsible for the monomer to adapt to a *syn*-or *anti*-conformation in the solid state is the size of the substituent in the 2-position of the Mepy ring.

4 Conclusions

Within a First-principles Bottom-up (FPBU) strategy, the computed macroscopic magnetic susceptibility χ(T) curves of bis(2-bromo-3-methylpyridine)dibromo copper(II), **1**, and bis(2-chloro-3-methylpyridine)dichlorocopper(II), **2**, agree with the experimentally observed dominant ferro- and antiferromagnetic behavior, respectively.

The computed magnetic topology of **1** consists of ferromagnetic chains ($J(d_2) = 1.16$ cm^{-1}) along the *b*-crystallographic axis, which then weakly interact (−0.11 and 0.13 cm^{-1}) giving rise to magnetic planes. For **2**, the strongest exchange coupling is antiferromagnetic and generates dimers ($J(d_1) = -2.37$ cm^{-1}) that, in turn, weakly interact (0.48, −0.29, and −0.20 cm^{-1}) to form double-decker magnetic planes. In both crystals, the 2D planes pile up along the third dimension showing no magnetic coupling between planes. The ferromagnetic d_2

radical-pair in **1** is a clear through-space Cu-Br···Br–Cu interaction, while the antiferromagnetic d_1 in **2** shows a mixture of through-space Cu···Cu, Cu···Cl, and Cl···Cl exchange pathways.

For simulation purposes, only the largest J_{AB} magnetic interactions are required to numerically reproduce the magnetic susceptibility as a function of temperature data. This is in agreement with the fitting models put forward on the basis of geometrical considerations and used to experimentally reproduce the measured χ(T) data, namely a ferromagnetic chain model with Curie–Weiss interchain corrections for **1** and an antiferromagnetic dimer model for **2**. Therefore, the FPBU analysis quantitatively traces down the origin of the different magnetic behavior of **1** and **2** as due to the change in sign of their dominant magnetic interactions. We have been able to connect such a change in nature of the dominant magnetic interaction with a change in the conformation of the ligands, which converts from *anti* in bis(2-bromo-3-methylpyridine) (**1**) to *syn* in bis(2-chloro-3-methylpyridine) (**2**). The relationship between the orientation of the substituents on the pyridine rings (*syn* or *anti*) and the structure holds; dimers are generated by *syn*-conformations (e.g. **2**) and chains by *anti*-conformations (e.g. **1**). It appears that the key factor responsible for the monomer to adapt to a *syn*- or *anti*-conformation in the solid state is the size of the substituent in the 2-position of the Mepy ring.

References

1. Johnston DC, Johnson JW, Goshorn DP, Jacobson AJ (1987) Phys Rev B Condens Matter Mater Phys 35(1):219
2. Barnes T, Riera J (1994) Phys Rev B Condens Matter Mater Phys 50(10):6817
3. Eccleston RS, Barnes T, Brody J, Johnson JW (1994) Phys Rev Lett 73(19):2626
4. Schwenk H, Konig D, Sieling M, Schmidt S, Palme W, Luthi B, Zvyagin S, Eccleston RS, Azuma M, Takano M (1997) Physica B 237–238:115
5. Eccleston RS, Mutka H, Payen C (1997) Physica B 234–236:895
6. Garrett AW, Nagler SE, Barnes T, Sales BC (1997) Phys Rev B Condens Matter 55(6):3631
7. Garrett AW, Nagler SE, Tennant DA, Sales BC, Barnes T (1997) Phys Rev Lett 79(4):745
8. Herringer SN, Turnbull MM, Landee CP, Wikaira JL (2011) Dalton Trans 40:4242
9. Deumal M, Bearpark MJ, Novoa JJ, Robb MA (2002) J Phys Chem A 106:1299
10. Szabo A, Ostlund NS (1989) Modern quantum chemistry: introduction to advanced electronic structure theory. McGraw-Hill Inc., New York
11. Hohenberg P, Kohn W (1964) Phys Rev 136:B864
12. Clarke CS, Jornet-Somoza J, Mota F, Novoa JJ, Deumal M (2010) J Am Chem Soc 132:17817
13. Deumal M, Giorgi G, Robb MA, Turnbull MM, Landee CP, Novoa JJ (2005) Eur J Inorg Chem 23:4697
14. Vela S, Deumal M, Turnbull MM, Novoa JJ (2012) Polyhedron. doi:10.1016/j.poly.2012.07.085
15. Jornet J, Li L, Turnbull MM, Landee CP, Deumal M, Novoa JJ, Wikaira JL (2007) Inorg Chem 46:11254
16. Novoa JJ, Deumal M, Jornet-Somoza J (2011) Chem Soc Rev 40:3182–3212
17. Noodleman L (1981) J Chem Phys 74:5737
18. Noodleman L, Davidson ER (1986) Chem Phys 109:131
19. Jornet-Somoza J, Deumal M, Turnbull MM, Novoa JJ (2009) Polyhedron 28:1965
20. Parr EG, Yang W (1989) Density functional theory of atoms and molecules. Oxford University Press, New York
21. Becke AD (1988) Phys Rev A 38:3098
22. Becke AD (1993) J Chem Phys 98:5648
23. Lee C, Yang W, Parr RG (1988) Phys Rev B 37:785
24. Schafer A, Horn H, Ahlrichs R (1992) J Chem Phys 97:2751
25. Ditchfield R, Hehre WJ, Pople JA (1971) J Chem Phys 54:724
26. Frisch MJ et al (2009) Gaussian 09, Revision B.1. Gaussian, Inc, Wallingford
27. Shortsleeves KC, Dawe LN, Landee CP, Turnbull MM (2009) Inorg Chim Acta 362:1859
28. Awwadi F, Willett RD, Twamley B (2011) Cryst Growth Des 11:5316
29. van Albada GA, Tanase S, Mutikainen I, Turpeinen U, Reedijk J (2008) Inorg Chim Acta 361:1463
30. Awwadi FF, Willett RD, Haddad SF, Twamley B (2006) Cryst Growth Des 6:1833
31. Espallargas GM, van de Streek J, Fernandes P, Florence AJ, Brunelli M, Shankland K, Brammer L (2010) Angew Chem Int Ed 49:8892
32. Lah N, Leban I (2010) Struct Chem 21:263
33. Singh P, Jeter DY, Hatfield WE, Hodgson DJ (1972) Inorg Chem 11:1657
34. Duckworth VF, Stephenson NC (1969) Acta Crystallogr Sect B Struct Crystallogr Cryst Chem 25:2245